# A highly sensitive multi-element HgCdTe e-APD detector for IPDA lidar applications

Jeff Beck[1], James McCurdy, Mark Skokan, Chris Kamilar, Richard Scritchfield, Terry Welch, Pradip Mitra, Xiaoli Sun*, James Abshire*, Kirk Reiff**

DRS Technologies, Network and Imaging Systems, Inc.
P.O. Box 740188
Dallas, TX 75374
*****NASA Goddard Space Flight Center
Greenbelt, MD 20771

**Analog/Digital Integrated Circuits
740 Florida Central Pkwy, Suite 1024, Longwood, FL 32750

## ABSTRACT

A 16 element HgCdTe e-APD detector has been developed for lidar receivers that has significant improvements in sensitivity in the spectral range from < 1μm to 4 μm. A demonstration detector consisting of a 4x4 APD detector array, with 80 μm square elements, a custom CMOS readout integrated circuit (ROIC), a closed cycle cooler-Dewar, and support electronics has been designed, fabricated, and tested. The custom ROIC design provides > 6 MHz bandwidth with low noise and 21 selectable gains. Ninety-six arrays were fabricated with 69% of the arrays meeting the dark current spec in the center 4 pixels at 10 V bias where the APD gain was expected to be around 150. Measurements to 12 V on one array showed APD gains of 654 with a gain normalized dark currents of 1.2 fA to 3.2 fA. The lowest dark current array showed a maximum dark current of 6.2 pA at 10 V and 77 K. The 4.4 μm cutoff detector was characterized at an operating temperature of 77K with a 1.55 μm, 1 μs wide, laser pulse. The photon conversion efficiency at unity gain was 91%. The mean measured APD gain at 77 K was 308 at 11V, the responsivity was 782 μV/pW, the average NEP was 1.04 fW/Hz$^{1/2}$. The bandwidth was 6.8 MHz, and the broadband NEP was 2.97 pW. This detector offers a wide spectral response, high dynamic range, and substantially improved sensitivity and lifetime for integrated path differential absorption (IPDA) lidar measurements of atmospheric trace gases such as CO2 and CH4.

**Keywords:** Avalanche photodiode, CO2, lidar, HgCdTe, APD, excess noise factor, NEP, IPDA, dynamic range

## 1. INTRODUCTION

NASA Goddard Space Flight Center (GSFC) is currently developing an integrated path differential absorption (IPDA) lidar that measure the column absorption of CO2 at 1572 nm, and CH4 at 1651 nm as candidates for NASA's Active Sensing of CO2 Emission over Days, Nights, and Seasons (ASCENDS) space mission. Both the CO2 and CH4 lidar measurements have been demonstrated from aircraft. One of the major technical challenges for the ASCENDS mission has been the lidar detector, that ideally has high photon sensitivity in this spectral region, a large linear dynamic range, along with a long in-space operational lifetime.

We have adapted the DRS HgCdTe e-APD detector for this application. The HgCdTe electron avalanche photodiode (e-APD) is a unique APD that provides high gain and high sensitivity from the visible to IR regions. This detector is attractive since its gain is nearly "noiseless" (the excess noise factor is close to unity) and is very uniform. It can provide analog response with sensitivities in the photon counting level from the visible to the mid-IR. This offers improved sensitivities for lidar receivers as well as for other electro-optical systems applications.

[1] jdbeck@drs-rsta.com

Sensors and Systems for Space Applications VI, edited by Khanh D. Pham, Joseph L. Cox, Richard T. Howard, Genshe Chen, Proc. of SPIE Vol. 8739, 87390V · © 2013 SPIE · CCC code: 0277-786X/13/$18 · doi: 10.1117/12.2018083

The HgCdTe APD, detector design is based on the highly successful High Density Vertically Integrated Photodiode (HDVIP®) architecture. The HDVIP device is a front-side illuminated, cylindrical, p-around-n photodiode that is formed around a small via in the HgCdTe, shown in Figure 1, where the via serves as the interconnect conduit between the n-side of the photodiode and the input to the readout circuit.[1] The HDVIP structure is currently employed in MWIR and LWIR staring arrays in production at DRS. The keys to the success of this architecture are: 1) interdiffused CdTe passivation of both surfaces for low 1/f noise, 2) thermal cycle reliability that is detector and array size independent, 3) low defects due to diode junction orientation with respect to threading dislocations, 4) front side illumination for high quantum efficiency into the visible region, Figure 2, and good MTF.

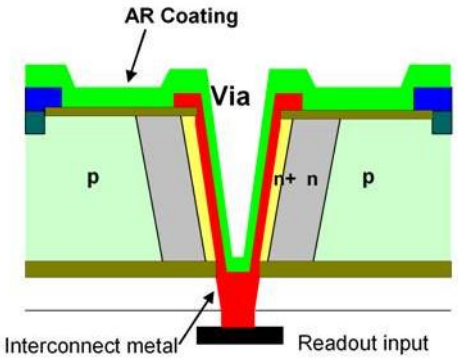


Figure 1 HDVIP cross section. As an e-APD the p region is the absorption region and the n- region is the multiplication region.

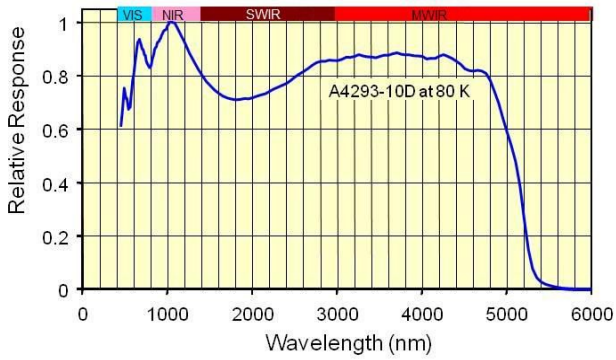


Figure 2 Broad spectral response from visible to MWIR is characteristic of front side illuminated HDVIP detectors.

For APD operation the reverse bias is increased until an electric field sufficient for avalanche multiplication is achieved. At a few volts bias, the n- region becomes fully depleted. Photo-electrons generated in the p region diffuse to the n region, which is the multiplication region. Multiplication occurs as the electrons transverse the high field depletion region as shown in Figure 3. A unique feature of the HgCdTe e-APD is that holes generated in the multiplication region, for all practical purposes, do not multiply which results in an ideal k = 0 APD where k is the hole to electron ionization coefficient ratio. Another unique feature of the HgCdTe e-APD is that the multiplication process is largely deterministic which results in an excess noise factor near 1.0.

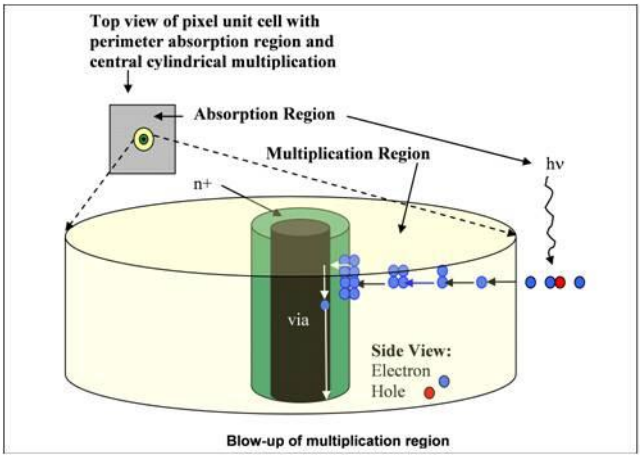


Figure 3 Cylindrical e-APD with a magnification of the multiplication region. Photo electrons generated in the p-type absorption regions diffuse to the central multiplication region. Holes generated, not shown, simply drift back to the p-region without multiplication.

The HgCdTe e-APD has shown high, uniform, exponential gain without breakdown (where the gain goes to infinity and the bandwidth goes to zero), as shown for a 4.3 μm cutoff array in Figure 4.[2] Also, the HgCdTe e-APD exhibits a gain independent excess noise factor, as shown in Figure 5.[2] These characteristics, exponential gain without breakdown, and a gain independent excess noise factor are predicted for an "ideal" k=0 APD. The near 1.0 excess noise factor is the result if a deterministic (history dependent) ionization process.

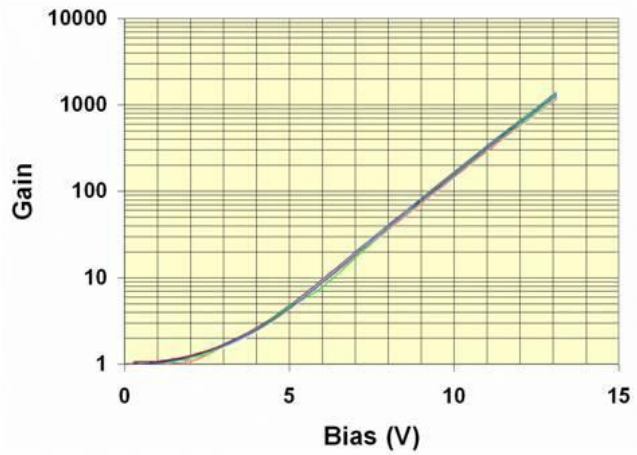


Figure 4 APD gain vs. bias @ 77K on 53 pixels in an 8x8 4.3 μm cutoff wavelength array. Gain is 1270 @ 13.1V σ = 4.5% Ref. [2]

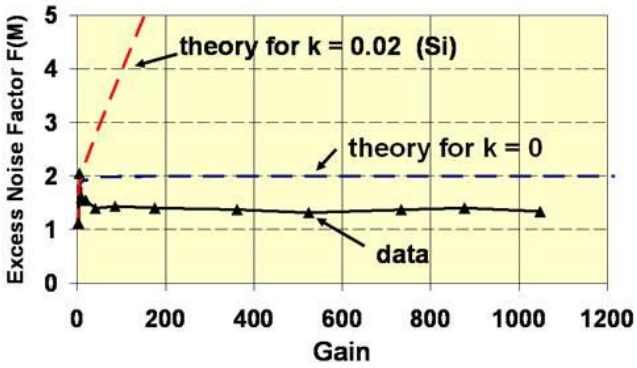


Figure 5 Gain independent excess noise factor with value close to 1.0 Ref. [2]

This performance has been realized in large area array formats. Range gated imaging, 128x128 40 μm pitch, focal plane arrays (FPAs) demonstrated sub 0.5 photon noise equivalent input sensitivities with APD gains as high as 946 as shown in Figure 6 and Figure 7.[3] Gated imagery was demonstrated with these FPAs, as illustrated in Figure 8 and Figure 9, with range to targets as long as 9 km.

Linear mode single photon detection with high single photon signal to noise ratio, average value of 13.7, less than 1ns jitter, and a photon detection efficiency near 50% has been demonstrated in a 2x8 array operating at an APD gain near 500 as shown in Figure 10.[4]

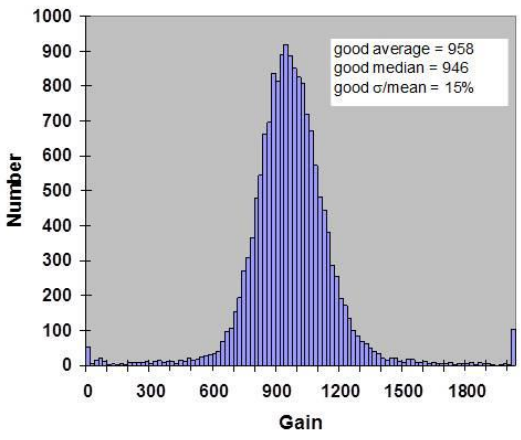


Figure 6 Gain of Gated 128x128 FPA 3A at 11 V Ref. [3]

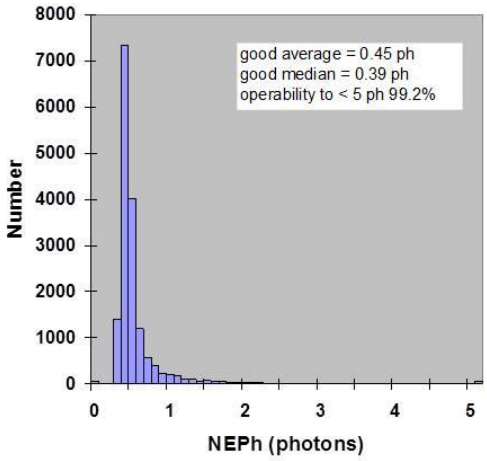


Figure 7 NEPh of Gated 128x128 FPA 3A at 11 V Ref. [3]

Figure 8 Visible image of water tower at 3.4 km with light pole in front. Ref. [4]

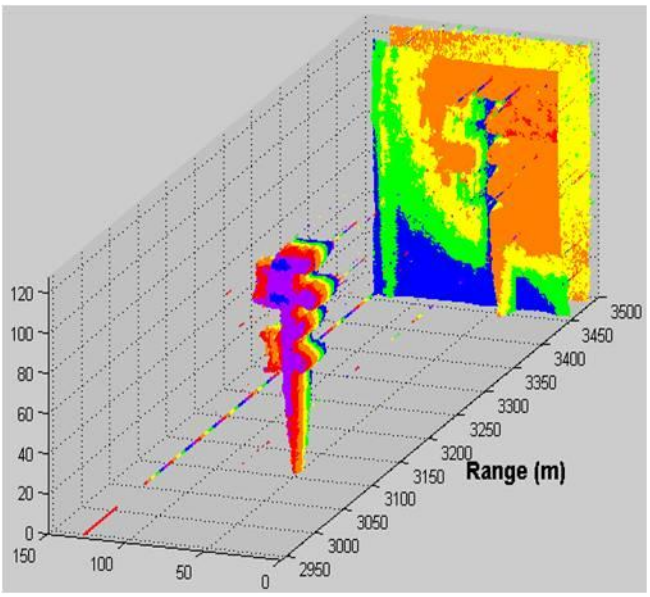


Figure 9 Reconstructed 3D image of light pole and water tower obtained by successive gated images that moved the 100ns gate through the scene. Ref. [4]

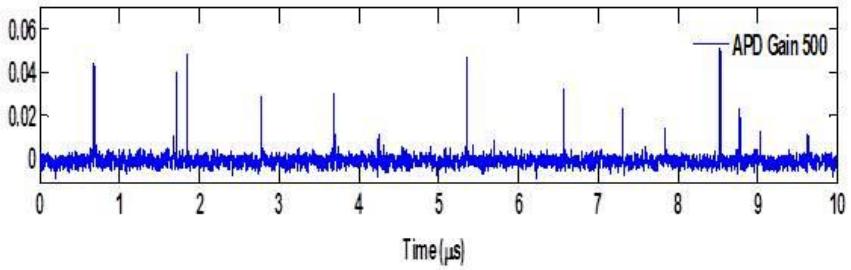


Figure 10 High single photon signal to noise ratio at APD gain of 500 [4]

## 2. DESIGN OF LIDAR DETECTOR

### 2.1 Requirements

This application is for an IPDA lidar that transmits 1 μs wide laser pulses with ~50 nsec rise times and so the design goal was to achieve an optimized noise equivalent power (NEP) for a bandwidth of 3-8 MHz. Based on simulations of ROIC performance discussed in Section 2.3, assumed detector quantum efficiency and a dark current, and Dewar optics transmission, we calculated the expected system NEP as a function of APD gain shown in Figure 11 for the baseline ROIC gain setting. This modeling showed that with a conservative set of assumptions an NEP of < 5 fW/Hz$^{1/2}$ could be achieved with conservative APD gains of ~ 100 with a gain normalized dark current (GNDC) of less than 64 pA, a 9.8 MHz bandwidth, and low noise TIA preamp with a gain of 331 KV/Amp. Enhanced performance was expected at higher APD gains and APD gains > 200 were expected along with lower dark currents.

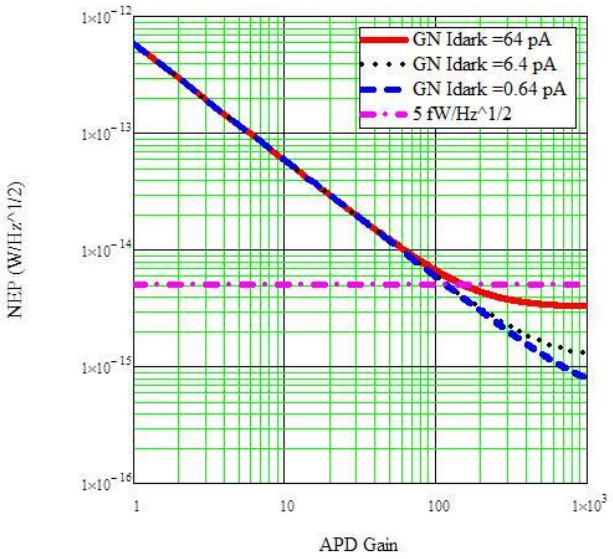


Figure 11 Predicted NEP for 9.8 MHz bandwidth

## 2.2 Array and Fanout

The array consisted of a 4x4 arrangement of pixels, with each pixel a square with a 80 μm side length.. The array is fabricated on a $Si0_2$/Si fanout that provides connections from the array to bond pads for interconnect to the ROIC. The array is surrounded by a ring of guard diodes surrounded by a substrate contact ring. The fanout metal layout for the array section is shown in Figure 12. Each pixels consists of 4 APDs, in a 2x2 arrangement, connected in parallel be means of underlying metallization on the fanout shown in Figure 13. A finished HgCdTe APD array is shown in Figure 14. The fanout was designed to provide a minimum stray input capacitance from the detector, to the bond pads. To do this, minimal trace lengths and trace widths, and small bond pads, were used.

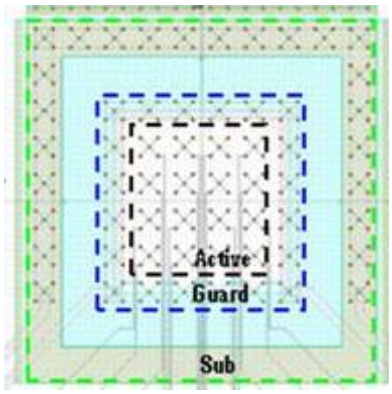


Figure 12 Fanout array design layout

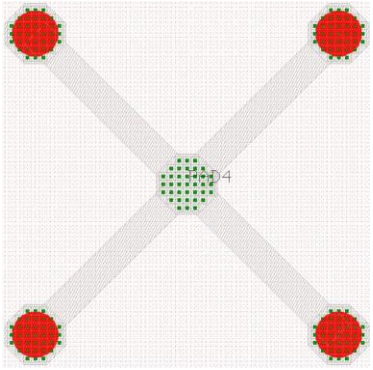

Figure 13 80 μm pitch 2x2 APD interconnect on fanout

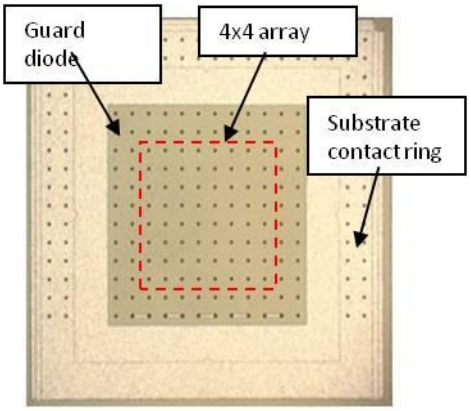


Figure 14 Finished 4x4 pixel array with 2x2 APD unit cells

## 2.3 Preamplifier (ROIC)

The ROIC is a custom CMOS design that uses 0.18 μm design rules. The unit cell, shown in Figure 15, consists of a resistive transimpedance amplifier (RTIA) connected to the cathode of the APD that provides signal input. Three selectable feedback resistors set the option of 7 transimpedance gain values. There is also the option of running in a capacitive transimpedance amplifier (CTIA) mode. The preamp is followed by a sample and hold circuit and a post-amp buffer stage with three selectable gain settings of 1, 2 and 4 V/V. The sample and hold is used in the CTIA mode. The combination of the preamp and post amp gain selections results in 21 possible full path transimpedance gains in the design that range from 47.7 kΩ to 1325 kΩ, a factor of 27.8. The design baseline was a full path gain of 331 kΩ with a 1x buffer gain setting. End to end performance simulations were carried out which assumed a worst case input capacitance. These simulations predicted that the bandwidth would range from 21.9 MHz at the lowest gain to 8.9 MHz at the highest gain. The baseline design gain was 331 kΩ at 80K; the predicted full path integrated noise was 336 μV; the 3dB signal bandwidth was 9.77 MHz; and the shot noise was 115.2 $fA/Hz^{1/2}$ at 100 KHz. The noise bandwidth was predicted to be 1.17 times the signal bandwidth.

The ROIC passed room temperature design verification testing at 25 C in RTIA mode with measured performance very close to simulation predictions as shown in Table 1. Figure 16 shows the 21 measured gains for all 16 channels. Figure 17 shows the pulse rise time, with the 320 KΩ 1x post amp gain setting, which implies a bandwidth of 9.2 MHz which is close to the predicted cold value of 9.8 MHz. Dynamic range measurements showed a 2V peak to peak swing. With an adjustable APD gain from 1 to 300 and the minimum to maximum ROIC gain, the dynamic range is expected to be greater than 71 dB from the noise level.

At DRS the ROIC was tested with a detector array. Proper operation, gain setting functionality, noise, and bandwidth were verified. With an 8x gain buffer board, the measured broadband noise with the baseline preamp gain settings was 302 μV which is lower, than the predicted simulation value of 336 μV. The rise time with this gain setting was 51 ns for a bandwidth of 6.8 MHz.

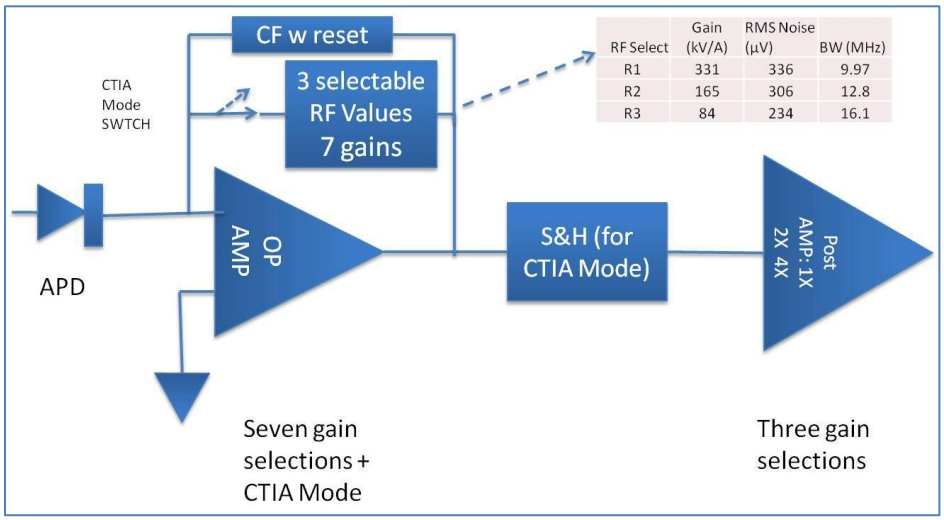


Figure 15 ROIC unit cell block diagram

**Table 1 ROIC Gain and bandwidth measurements summary at 25 C**

| Design Parameter | Design Goal (Ideal Values) | Mean Measured (@ T ~ 25C) |
|---|---|---|
| Preamp Gain 6, Postamp 1X | 320 Kohms | 321.71 Kohms |
| Preamp Gain 5, Postamp 1X | 160 Kohms | 161.36 Kohms |
| Preamp Gain 4, Postamp 1X | 106.57 Kohms | 107.26 Kohms |
| Preamp Gain 3, Postamp 1X | 80 Kohms | 81.49 Kohms |
| Preamp Gain 2, Postamp 1X | 64 Kohms | 64.98 Kohms |
| Preamp Gain 1, Postamp 1X | 53.33 Kohms | 53.98 Kohms |
| Preamp Gain 0, Postamp 1X | 45.71 Kohms | 46.29 Kohms |
| Post Amp Gain 2X | 2.0 V/V | 2.018 V/V |
| Post Amp Gain 4X | 4.0 V/V | 4.010 V/V |

| Design Parameter | Design Model @ Cryo | Measured * @ T ~ 25C |
|---|---|---|
| Preamp Gain 6, Postamp 1X | 9.77 MHz ** | 8.55 MHz |
| Preamp Gain 5, Postamp 1X | 12.77 MHz | 12.42 MHz |
| Preamp Gain 4, Postamp 1X | 20.80 MHz | 21.13 MHz |
| Preamp Gain 3, Postamp 1X | 16.10 MHz | 17.44 MHz |
| Preamp Gain 2, Postamp 1X | 20.69 MHz | 22.10 MHz |
| Preamp Gain 1, Postamp 1X | 18.47 MHz | 20.45 MHz |
| Preamp Gain 0, Postamp 1X | 21.90 MHz | 22.85 MHz |
| Output Noise***, Preamp Gain 6, Postamp Gain 4X (~ **1300Kohms**) | 1.036 mVrms | 0.94728 mVrms (mean of 16 channels, test set noise NOT RSS'ed out) |

### 2.4 Dewar and Optics

A closed cycle, reconfigurable, Dewar with a 1.5 watt cryocooler was selected for operation at temperatures near 80K. The cold shield was designed to accommodate a F/1.5 optical cone and a 25.4 mm diameter cold filter. A 1.2 to 1.8 μm bandpass filter with OD4 blocking from 3 to 5 μm was selected for testing with 1.55 μm laser signals at DRS. The Dewar had two multi-pin connectors for I/O.

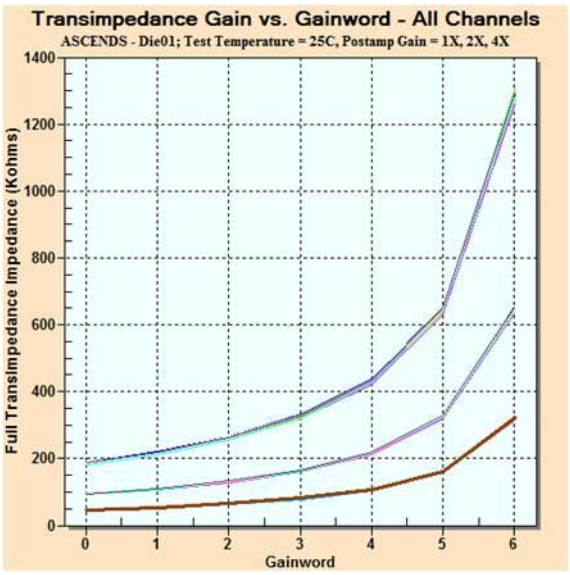


Figure 16 Measured transimpedance gain at room temperature for the 7 RTIA gain settings and 3 post amp gain settings

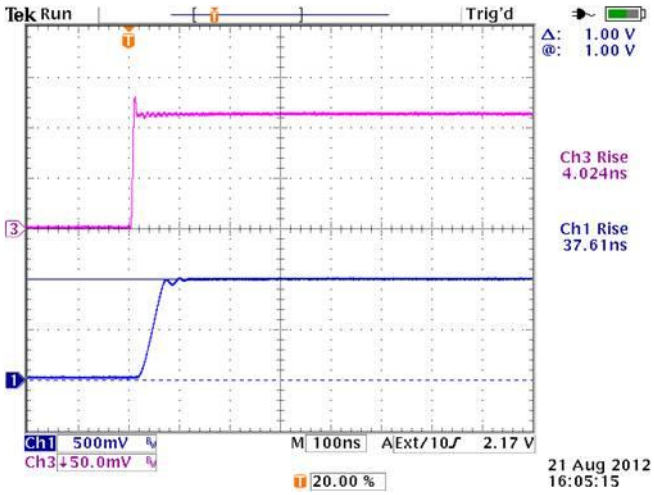


Figure 17 Measured step response rise time at room temperature for RTIA gain setting of ~ 320 kΩ and post amp gain setting of 1.

### 2.5 Electronics and Software

A custom set of 4 electronic printed circuit boards were designed and fabricated: 1) an internal Dewar board; 2) an external Dewar interface card with buffers for the analog signals; 3) a second external Dewar interface card for digital control and power; 4) a power, command, and control, side-board. The internal Dewar board holds the 68 pin LCC and provides the electrical interface between the LCC and the two Dewar connectors. The two external Dewar interface cards attach directly to the two Dewar connectors. The side-board is connected to the interface cards with ribbon cables. FPGA code and software were written to provide a control from using a laptop PC connected by a USB port to the side-board. Two analog buffer cards were fabricated: one with a 1x gain into 50 Ω and another with an 8x gain.

## 3. 4X4 ARRAY FABRICATION AND TEST

A fabrication lot was run with 96 4x4 arrays on 16 HgCdTe chips. A finished array is shown in Figure 14. The arrays were screened by measuring dark current voltage data out to 10 V on the center four pixels of each array at 77 K. Sixty-six arrays (69%) met the dark current requirement in the center four pixels. Eleven of these were selected for full 16 pixel characterization. Five "perfect" arrays were found in which all pixels met 6.4pA maximum GNDC spec at 10 V where the APD gain was assumed to be around 160.[2] The data are summarized in Table 2. Four of these five arrays had pixels with gain normalized dark currents no higher than 67 fA. The center 4 pixels in these 4 arrays had gain normalized dark currents less than 8.6 fA, that is almost 0.1% of the baseline design requirement. Figure 18 and Figure 19 show the GNDC maps at 10 V for arrays 4E and 7C.

Gain and dark current were measured as a function of bias on several arrays. Array A8052-2C had a gain of 173 at 10 V. The GNDC at 10 V was about 4 fA, which is well below the flow down baseline requirement of 6400 fA. A8052-2A had a gain at 10 V of 157 and a GNDC of 18 fA. Another fanout array, A8052-15D, was measured for gain and dark current out to 12 V. The data shown in Figure 20 and Figure 21 reveal a gain of 654 at 12 V, and a GNDC of 1.2 to 3.2 fA at 12 V. In conclusion, based on dark current and gain measurements, the 4x4 fanout lot produced excellent dark current

[2] The gain of 160 used in the calculation of gain normalized dark current is based on measured gains from 157 to 173 on two arrays 2A and 2C from this lot. It should be fairly close to the gain for all arrays in the lot since the cutoffs are the nearly the same (4.27 to 4.35 μm).

results with very good yield. Based on the model shown in Figure **11**, noise bandwidth normalized system NEPs of 1 $fW/Hz^{0.5}$ should be possible.

**Table 2 Gain normalized dark current at 10 V of 5 "perfect" fanout arrays (gain of 160 assumed)**

| Array | Median GNDC (fA) | Max GNDC (fA) | Max GNDC (center 4) (fA) |
|---|---|---|---|
| 4E | 1.64 | 3.94 | 1.3 |
| 11D | 1.43 | 20.4 | 8.53 |
| 7C | 0.883 | 8.11 | 1.7 |
| 13E | 3.49 | 66.8 | 8.13 |
| 16B | 5.46 | 7540 | 8.06 |

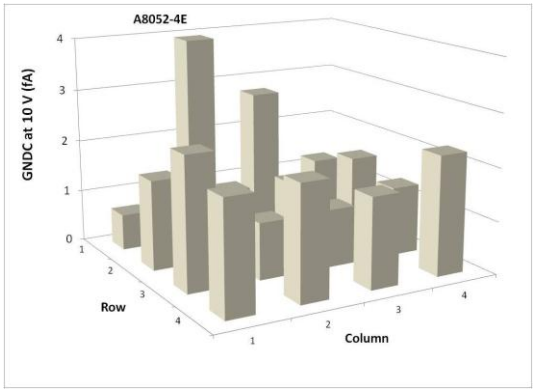


Figure 18 Gain normalized dark current map for array A8052-4E at 77 K at 10 V. Assumed APD gain = 160. Median gndc: 1.64 fA. Max gndc: 3.94 fA.

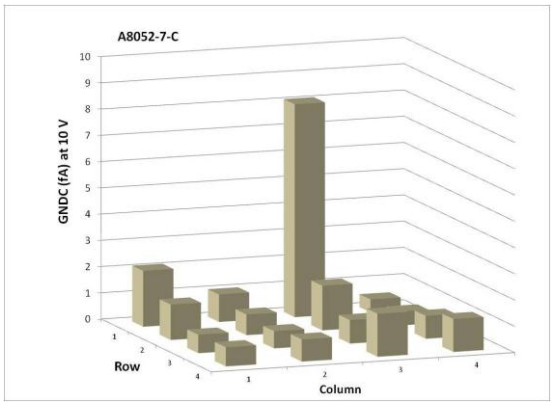


Figure 19 Gain normalized dark current map for array A8052-7C at 77 K at 10V. Assumed APD gain = 160. Median gndc: 0.88 fA. Max gndc: 8.11 fA.

## 4. RESULTS FROM DETECTOR EVALUATION

### 4.1 Sensor Chip Assembly

The five selected fanout arrays were integrated with tested ROIC chips in a 68 pin LCC. The layout is shown in Figure 22 and a finished assembly is shown in Figure 23.

### 4.2 System Integration

The 4x4 array detector system, consisting of the Dewar, cooler, optics, electronics boards, and SCA, was assembled. The system in the test configuration is shown in Figure 24. The photograph shows the calibrated fiber laser signal source.

### 4.3 Test Results

The overall operation was verified using a pathfinder array A8052-3B. Functionality of the electronics and ROIC was verified, and minor system issues were addressed and solved. The first set of data was measured on array A8062-4E. The system test conditions are summarized in Table 3.

We first performed some basic characterization measurements. Shown in Figure 25 is the measured APD gain vs. bias on one of the pixels, pixel 9 (row 3, column 1) at 77K. The gain at 10 V was 141 and at 11 V it was 297. The photon-

to-electron conversion efficiency, CE, at unity gain is plotted in Figure 26.[3] The CE was calculated from the measured signal data at a bias of 0.5 V where the APD gain is 1. The calculation assumes the expected end-to-end gain of 330kV/Amp based on the measured room temperature values with a predicted 3% increase at cryo. The data show an average calculated CE of 91.0% and a 1.5% σ/mean uniformity.

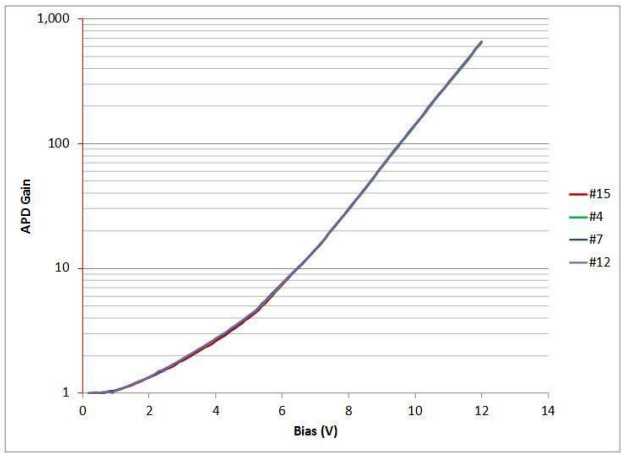


Figure 20 Gain vs. voltage on four pixels from detector array A8052-15D to 12 V. Gain of 654 at 12 V.

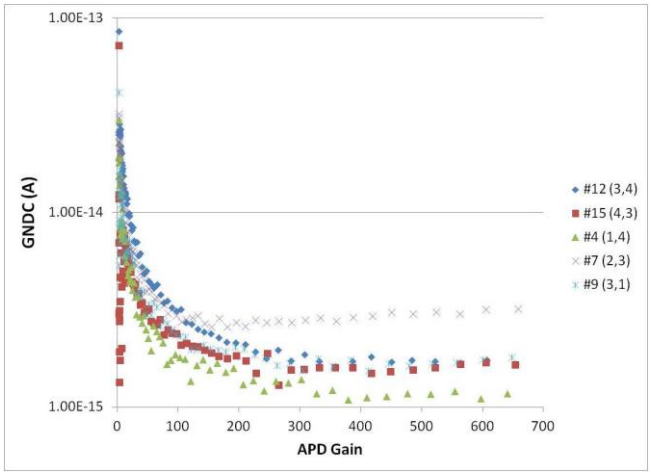


Figure 21 Gain normalized dark current density vs. gain on pixels from detector array A8052-15D

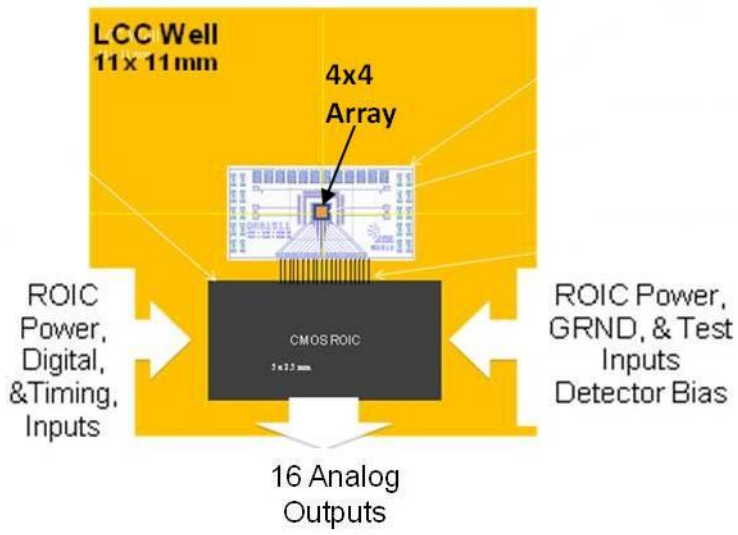


Figure 22 Sensor chip assembly layout. The fanout array is centered in the LCC.

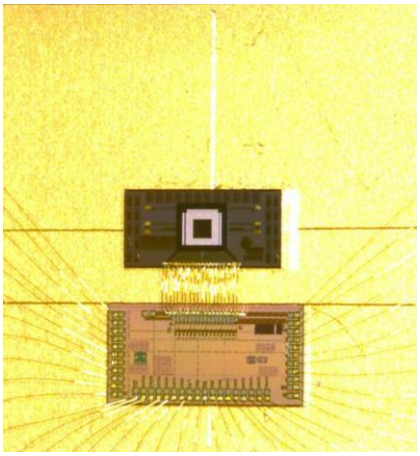

Figure 23 Sensor chip assembly in 68 pin LCC. The fanout array is centered in the LCC well.

[3] The photon to electron conversion efficiency, CE, is defined as the product of the photon absorption efficiency, fill factor and electron collection efficiency. The CE is the net overall pixel "quantum efficiency".

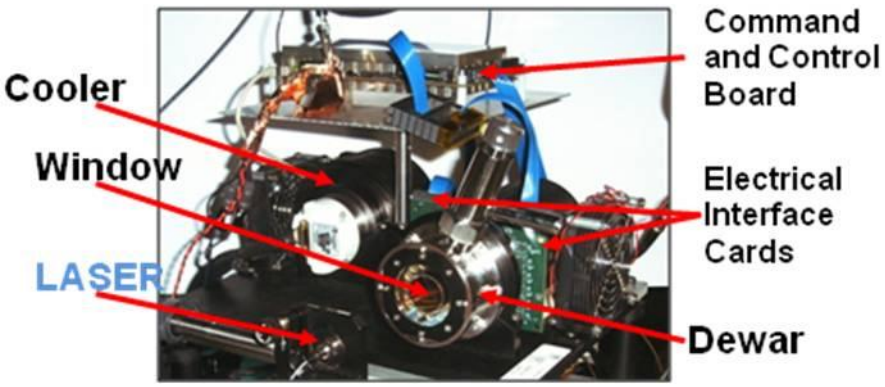


Figure 24 The 4x4 APD array detector system in its test configuration

**Table 3 Test conditions for 11 V NEP data**

| *Parameter* | *Value* | *Units* |
|---|---|---|
| Signal wavelength | 1.55 | μm |
| Signal pulse width | 1 | μs |
| Signal amplitude | < 2-100 | nW |
| Operating temperature | 77 | K |
| ROIC Preamp gain | 330 | kW |
| ROIC postamp gain | 1 | V/V |
| Dewar buffer card gain into 1MΩ | 8 | V/V |
| Cold Filter pass band | 1.2-1.8 | μm |
| Cold filter transmission @ 1.55 μm | 86 | % |
| Cold filter blocking 3-5 μm | OD4 | NA |
| Dewar window transmission | 97 | % |

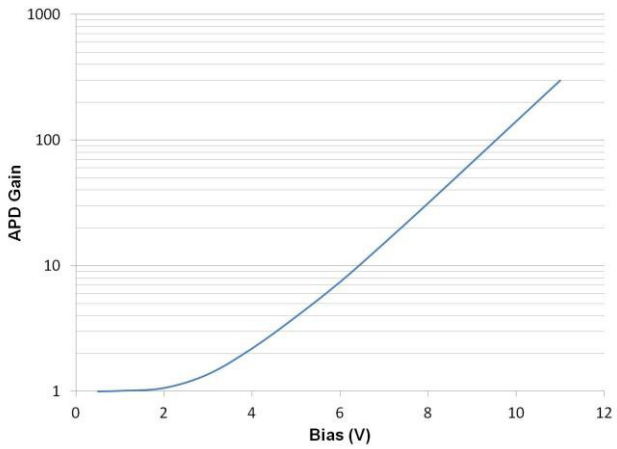


Figure 25 Gain vs. Bias for A8052-4E pixel 9 at 77 K.

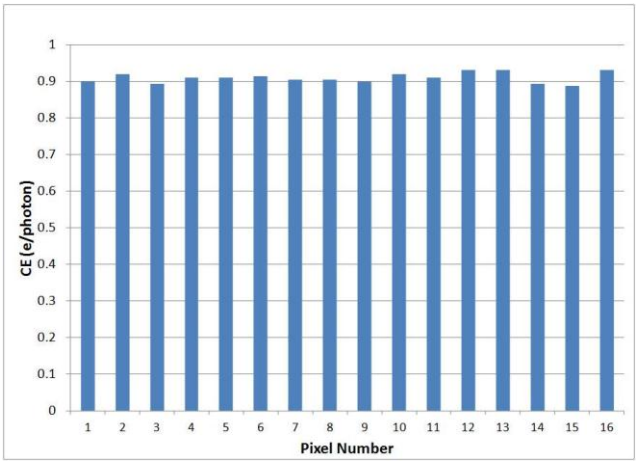


Figure 26 Calculated CE vs. pixel number at unity gain 77 K.

The rise times were measured on all 16 pixels at 77 K with a 10 V bias applied (the APD bandwidth is independent of bias above about 3V). The rise times varied from 49.6 ns to 51.8 ns with an average of 50.9 ns. Shown in Figure 27 is the measured gain at 10 V and 11 V on all pixels at 77 K. At 11 V the average gain was 307.8 with a σ/mean of 1.2%. At 10 V the gain dropped to 146.0 with a σ/mean of 1.3%

We measured the system NEP at APD biases of 10V and 11 V at 77 K with an external buffer gain of 8 V/V. Shown in Figure 28 is the system responsivity at 11 V in μV/pW vs. pixel. The average is 782.0 μV/pW with a 1.8% σ/mean. The corresponding detector responsivity at 11 V was 355 A/W. The average broadband NEP at 11 V was 2.97 pW. The estimated NEP/$Hz^{1/2}$ is calculated by dividing the NEP by the noise bandwidth which is estimated to be 1.2 times the signal bandwidth. The NEP for each pixel, shown, in Figure 29, indicates an average NEP at 11 V of 1.04 fW/$Hz^{1/2}$ with a 3.8% σ/mean and 100% pixel operability with no pixel having an NEP less than 1.12 fW/$Hz^{1/2}$.

At 10 V the APD gain decreased to 145 and the NEP increased to 2.20 fW/$Hz^{1/2}$. This indicates that the NEP is changing directly with APD gain. Therefore, further reduction in the NEP is expected with increased bias beyond 11 V.

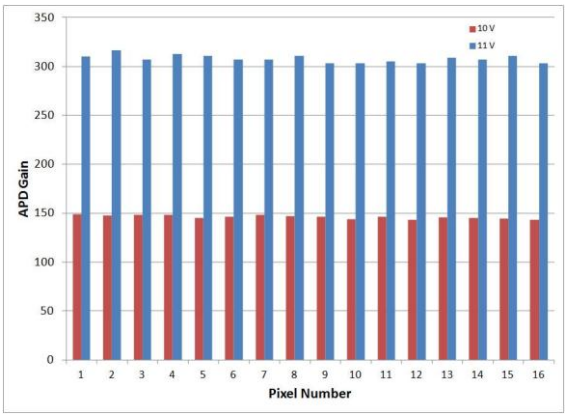


Figure 27 APD gain at 10V and 11 V vs. pixel at 77K for array A8052-4E

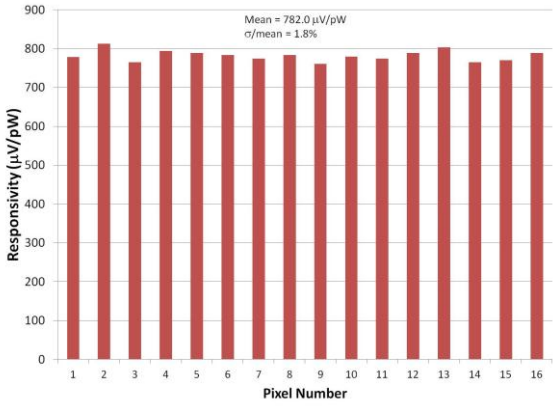


Figure 28 System responsivity at 1.55 μm @ 11 V vs. pixel at 77K for array A8052-4E with buffer gain of 8

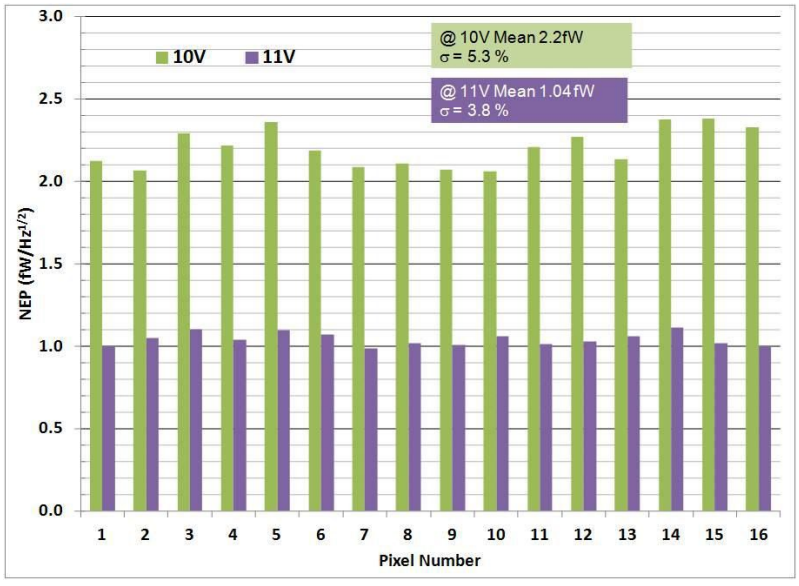


Figure 29 System NEP vs. pixel at 10 V and 11 V bias at 77 K (A8052-4E)

## 5. SUMMARY

We have developed and characterized a new, highly sensitive, 4x4 HgCdTe e-APD array optimized for 1 μs lidar pulse detection and packaged with Dewar, cooler, and electronics. The APD fabrication process demonstrated a high array yield based on high bias dark current measurements.

The measured performance at 77 K is summarized Table 5 for the set of conditions listed in Table 4. The 1st array has an average NEP of 1.04 fW/Hz$^{1/2}$ at 11V bias with 100% pixel operability and very good gain, responsivity, and NEP uniformity. The measured bandwidth was > 6 MHz and the NEP was almost a factor of 5 better than the design goal. The dynamic range for the minimum to maximum ROIC gain and a variable APD gain from 1 to 300 is 72 dB, measured from the noise level. The measurement results showed good agreement with performance predictions. Based on measured dark current-voltage data we expect improved performance at higher APD gains. We expect similar performance will be seen in the other 4 candidate arrays.

We plan to demonstrate this detector in IPDA lidar measurements later this year.

**Table 4 Operating conditions for detector NEP characterization (Table 5)**

| Parameter | Value | Comment |
|---|---|---|
| FPA Temperature | 77 K | Initial setting during cooler check-out |
| ROIC Gain | 331 kΩ | Predicted for 80 K (320 KΩ @ 300K) |
| ROIC post amp gain | 1 | |
| Buffer Gain | 8 | 50 Ohm load |
| Laser pulse width | 1 μs | |

**Table 5 System performance at 1.55 μm with Baseline RTIA Gain Setting**

| Parameter | Value | Comment |
|---|---|---|
| APD Bias | 11 V | Applied to all pixels |
| APD Gain | 308 | Average |
| NEP at 1.55 μm | 2.97 pW | Broadband NEP |
| NEP/Hz$^{1/2}$ | 1.04 fW/Hz$^{1/2}$ | Normalized to noise bandwidth |
| Responsivity at 1.55 μm | 782 μV/pW | At system output |
| Noise at 11 V | 2.32 mV | At system output (gain of 8) |
| System Noise (@ 0.5 V) | 2.41 mV | At system output (gain of 8) |
| Bandwidth | 6.8 MHz | 51 ns rise time |
| Noise bandwidth | 8.1 MHz | Based on predicted 1.2 factor |
| Dynamic Range (dB) | 72 | APD gain 1-300; min to max ROIC gain |

**Table 6 Modes and Gains for the ROIC and External Buffer Amplifier**

| ROIC Gains (kVolt/Amp for RTIA mode) | ROIC Post Amp gains (V/V) | Buffer board gains (V/V) into 50 Ohms |
|---|---|---|
| 47.68, 55.71, 66.90, 83.85, 110.55, 165.99, 330.94, CTIA (2.66μV/e) | 1, 2, 4 | 1, 8 |

## 6. FUTURE PLANS

We plan to characterize the 4 other SCAs. We also will measure the NEP at higher gains and biases settings of 12 V to 13 V. GSFC plans to integrate the delivered detector, Dewar, cooler, and electronics assembly into their airborne IPDA lidar and to demonstrate measurements of CO2 over horizontal paths and from an aircraft.

## 7. ACKNOWLEDGEMENTS

This work was supported by the NASA ESTO IIP-10 program managed by Parminder Ghuman and Irene Bibyk.

[1] J. Beck, C. Wan, M. Kinch, J. Robinson, P. Mitra, R. Scritchfield, F. Ma, and J. Campbell, "The HgCdTe Electron Avalanche Photodiode", IEEE LEOS Newsletter, 20(5), 8-12 (2006).
[2] J. Beck, C. Wan, M. Kinch, J. Robinson, P. Mitra, R. Scritchfield, F. Ma, J. Campbell, "The HgCdTe Electron Avalanche Photodiode", *J. Elecron. Mater.* 35(6), 1166-1173 (2006).
[3] J. Beck, M. Woodall, R. Scritchfield, M. Ohlson, L. Wood, P. Mitra, and J. Robinson, "Gated IR Imaging with 128x128 HgCdTe Electron Avalanche Photodiode FPA", Proc. SPIE, 654217, 1-17 (2007).
[4] J. D. Beck, R. Scritchfield, P. Mitra, W. Sullivan III, A. D. Gleckler, R. Strittmatter
Robert J. Martin, "Linear Mode Photon Counting with the Noiseless Gain HgCdTe e-APD", Proc. SPIE, 80330N, 1-15 (2011).